Surfing the Hippocampus Wave

Bartel, F.

2019

document version
Publisher's PDF, also known as Version of record

Chapter 1

Introduction

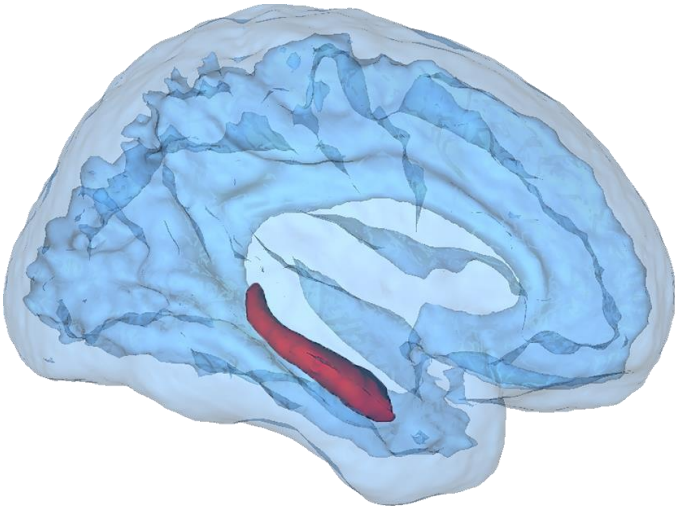

1.1. Clinical motivations

The brain is the central organ of the human nervous system, responsible for controlling all senses and body functions. The brain is protected by the skull and cerebrospinal fluid (CSF) and consists of the cerebrum, cerebellum and the brain stem which is connected to the spinal cord. The cerebrum is the largest part of the brain and is divided in left and right hemispheres. It is composed of grey (GM) and white matter (WM) and encompasses structures such as the thalamus, hippocampal formation, amygdala and basal ganglia, consisting of the caudate nucleus, putamen and globus pallidus (Fig. 1).

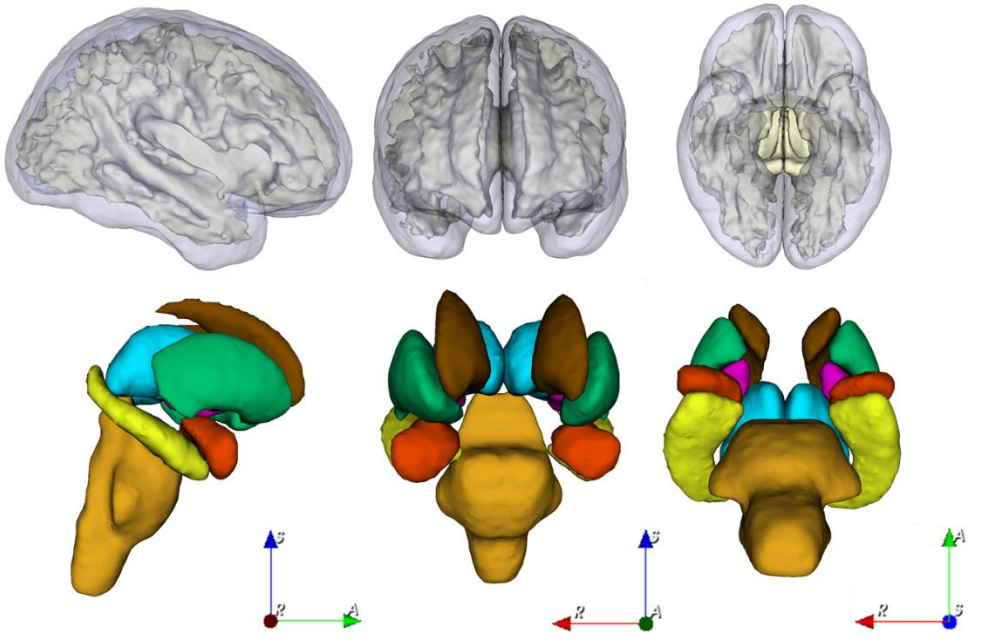

Fig. 1: Top row shows the cerebrum in which white matter is shown in dark blue. Bottom row are encompassed structures. Orange: brain stem; Yellow: hippocampus; red: amygdala; green: putamen; cyan: thalamus; brown: caudate nucleus; magenta: globus pallidus. S: superior; A: anterior; R: right. The Harvard-Oxford probabilistic atlas from FSL [1] in MNI152 template [2] space was converted to meshes.

The hippocampal formation is often referred to as archicortex. It consists of the dentate gyrus, cornu ammonis areas (CA1 to CA4), subiculum, fimbria, alveus, presubiculum, parasubiculum and the entorhinal cortex. The CA areas are known as the hippocampus proper. Sometimes, the presubiculum, parasubiculum and the entorhinal cortex are part of the term parahippocampal gyrus and are excluded from the hippocampal formation. Hippocampal subfields are illustrated in Fig. 2, in which a model created by [3] and [4].

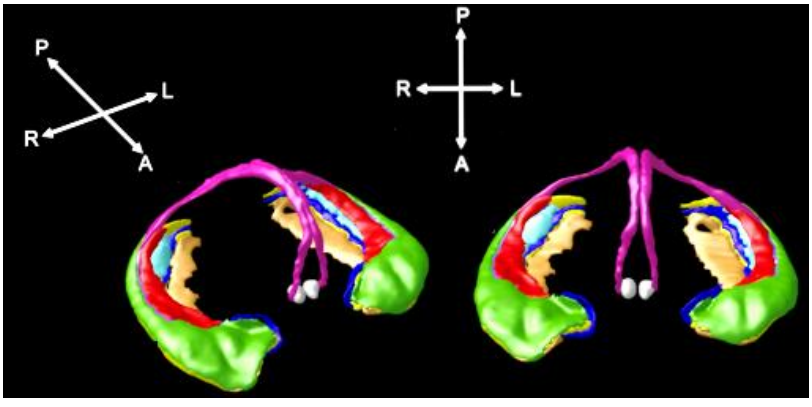

Fig. 2: A model of the hippocampal subfields, the fornix and mammillary bodies is shown [3,4]. Green: alveus; red: fimbria; pink: fornix; yellow: CA1; bright blue: CA2/3 (lies underneath the fimbria); cyan: CA4/dentate gyrus; dark blue: strata radiatum/lacunosum/moleculare; beige: subiculum; grey: mammillary bodies.

Usually, the term 'hippocampus' includes only the hippocampus proper and the dentate gyrus [5]. The hippocampal head, body and tail are marked in Fig. 3. The hippocampus plays an important role in neurogenesis, learning and memory functions [6]. Therefore, in brain image analysis, especially for neurodegenerative diseases, the anatomy of the hippocampus is extensively investigated. The central theme of this thesis is the accuracy by which the hippocampal shape can be determined from magnetic resonance imaging (MRI), and to determine in what extent it is possible to detect subtle hippocampal volume loss and other longitudinal shape changes. In the remainder of this thesis the term atrophy is used as a synonym for volume loss. Hippocampal atrophy is a result of cell degeneration leading to volume loss.

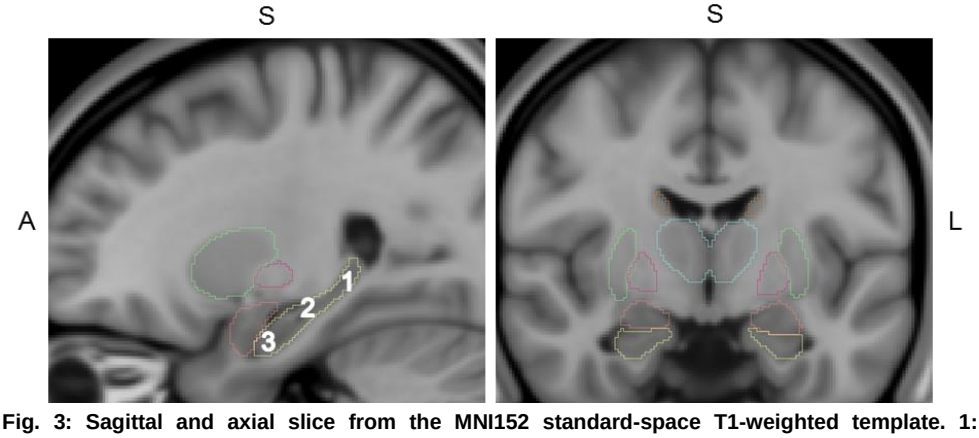

Fig. 3: Sagittal and axial slice from the MNI152 standard-space T1-weighted template. 1: hippocampal tail; 2: hippocampal body; 3: hippocampal head; red: amygdala; green: putamen; cyan: thalamus; brown: caudate nucleus; magenta: globus pallidus. The MNI152 template brain [2] is used and structures from the Harvard-Oxford probabilistic atlas from FSL [1] are shown.

Neurodegenerative diseases

In neurodegenerative diseases progressive degeneration and/or death of nerve cells leads to problems in brain functioning. Many neurodegenerative diseases exist, the most well-known ones are Alzheimer's disease (AD), Parkinson's disease, dementia with Lewy bodies, frontotemporal dementia, amyotrophic lateral sclerosis and Huntington's disease [7]. Multiple sclerosis (MS) is an inflammatory demyelinating disease which also causes neurodegeneration. This thesis mainly covers hippocampus anatomical changes associated with AD but also applications for MS. AD mainly affects elderly people and accounts for up to 75% of all dementia cases worldwide [8]. Worldwide, approximately 47 million people with age 60 or higher have been diagnosed with dementia and with the increasing age of the population, this number is expected to increase to 131 million by 2050 [9]. Of these 47 million people with dementia, 58% live in low- and middle-income countries. In Europe, approximately 10.5 million people and in north America approximately 5 million people suffer from dementia [9]. Only little is known about the cause of AD, but increased prevalence of amyloid plaques and neuronal tangles are prime suspects. Plaques are built due to abnormally folded amyloid beta and tau proteins [10]. Plaques and tangles block signalling from cell to cell and transport of molecules. Research to prevent amyloid deposition in the early stages of AD is therefore highly important. Early signs of cognitive impairment have been formalized in criteria for mild cognitive impairment (MCI), which in most patients is a transitional state before reaching the clinical threshold for dementia [11]. Most MCI patients develop AD with around 15% progressing to AD per year [12]. The hippocampus is often damaged in the early stages of AD. Other important structural imaging biomarkers in AD are derived from the neocortex (reduced cortical thickness) and regions such as the amygdala, thalamus and basal ganglia (volume loss) [13].

MS is an inflammatory disease of the brain and the spinal cord. It causes focal inflammatory demyelinating lesions and neurodegeneration in the GM can occur [14,15]. The prevalence of MS greatly varies per region and is highest in North America (140/100,000) and Europe (108/100,000) and lowest in east Asia (2.2/100,000) and sub-Saharan Africa (2.1/100,000). Demyelination is a result of an autoimmune response towards the myelin, in which immune cells attack the damaged myelin leading to inflammation of the tissue [16]. Furthermore, MS leads to whole brain atrophy [17] and GM atrophy in both the cortex and deep grey matter structures such as the thalamus, caudate nucleus and putamen [18,19], but also the hippocampus [20].

Volume loss quantification and clinical relevance

Changes to the brain caused by neurodegenerative diseases can lead to cognitive dysfunction such as loss of memory, thinking, reasoning and executive functioning. Such changes can have profound effects on the quality of life and therefore prevention and/or early detection of structural brain changes for treatment is of high importance.

These functional changes are often associated with tissue loss and hence to anatomical changes that are detectable with MRI. Measuring anatomical changes over time in vivo of structures such as the hippocampus is important to support diagnoses and to monitor the course of a disease. For clinical research organisations, which perform centralized image analysis in clinical treatment trials for the pharmaceutical industry, anatomical changes such as hippocampal volume changes are important biomarkers that are used as secondary outcome measures evaluating the efficacy of new drugs. A recent overview of completed trials with hippocampal volume change as an outcome measure can be found in [21].

MRI is usually the method of choice to make 3D images of brain anatomy because of its high resolution and its good soft tissue contrast. Shape and volume of the hippocampus can be obtained from a 3D brain MRI by delineating the hippocampus pixel by pixel and slice by slice, a process called segmentation. This can be done fully manually, fully automatically, or through some combination; more details are provided below. To determine hippocampal atrophy, the hippocampus needs to be segmented on longitudinal MRI scan pairs of the same patient. Compared to visual inspection of 3D MRI, volumetric segmentation provides a more precise quantification of brain structures and their longitudinal changes.

Hippocampal atrophy

It is well known that even in healthy subjects, hippocampal atrophy may occur. A systematic review and meta-analysis of longitudinal hippocampal atrophy in healthy aging subjects reported a mean annual hippocampal volume decline of 0.38% for subjects with a mean age <55 years, 0.98% for subjects between 55 and 70 years of age, and 1.12% for subjects ≥70 year [22]. Furthermore, even though the right hippocampus is known to be larger than the left hippocampus [23], left and right atrophy rates in healthy controls were not significantly different [24,25]. In AD, early findings based on longitudinal MRI-based volume measurements demonstrated increased annual hippocampal atrophy rates in aged matched subjects (70-89years old) with a change of −3.98% ± 1.92%/year in AD subjects compared a change of −1.55% ± 1.38%/year in controls [26]. A meta-analysis of hippocampal atrophy rates in AD reported similar atrophy rates with a mean annual hippocampal volume

decline of 1.41% for elderly controls and 4.66% for AD subjects [27]. The subjects of the studies included in this meta-analysis had mean ages ranging from 68 to 83 years. Another systematic review and meta-analysis in MCI, estimated mean hippocampal atrophy rates of 2.53% per year with mean ages per study ranging from 66 to 79 years [28]. In both MCI and AD, only small and non-significant differences in left and right hippocampal atrophy rates have been observed [24,25].

The absolute difference in annual hippocampal atrophy rates between healthy controls and MCI and AD subjects is approximately 1% and 3% respectively. Therefore, hippocampal atrophy measurement methods have to be highly accurate to support a diagnosis or to evaluate the efficiency of drugs correctly.

Quantification of radiation induced brain damage

Techniques to measure longitudinal shape changes on MR images were originally developed with the perspective to provide an automatic tool to quantify atrophy in neurodegenerative diseases. More recently, these developments have attracted the interest from radiotherapists to serve as a tool to analyse subtle changes to brain structures arising due to irradiation. In patients with brain tumours or brain metastases originating from extracranial tumours, brain radiotherapy is often the core treatment [29]. Every year, hundreds of thousands of patients worldwide receive brain radiotherapy, of whom around 50% die less than 6 months following brain irradiation, and 50-90% of the survivors develop cognitive dysfunction [30]. Radiation induced cognitive decline reduces the quality of life of patients, which is an important factor to account for in oncology. Until now, little is known about the pathophysiology of radiation induced cognitive decline [31]. Early radiation-induced brain damage, for instance loss of WM, reduction of oligodendrocytes, microvascular damage and neuroinflammation, can change into larger macrostructural brain changes over time, leading to long-term cognitive decline [29]. Furthermore, animal studies have shown that the neural stem cell (NSC) compartment in the dentate gyrus of the hippocampus is vulnerable to radiation and already small doses can damage it [32–36]. Therefore, having precise methods to measure radiation induced structural brain changes on MRI is highly important to reveal radiation sensitive brain regions and to better understand radiation induced cognitive decline.

Whole brain radiation therapy is the standard treatment to control brain metastases. It has shown improved survival but can also cause cognitive dysfunction in memory-related domains [37]. In the last decade, due to growing awareness of susceptibility of the hippocampus to radiation damage, hippocampal sparing techniques have been developed to limit cognitive dysfunction [38]. For such techniques accurate hippocampal segmentation is needed to reduce radiation in the hippocampal region

specifically. Several clinical trials are investigating the effectiveness of hippocampal sparing techniques (ClinicalTrials.gov identifiers: NCT01797159, NCT01780675, NCT02635009). One important biomarker for these trials is the determination of accurate hippocampal volume loss, using T1-weighted structural MRI. Therefore, an evaluation of methods to detect radiation induced hippocampal volume loss is of high importance in radiotherapy.

1.2. Technology and technological challenges

The general goal of this work is to develop, test and compare tools to efficiently quantify anatomical shapes (in particular the hippocampus) and determine their longitudinal changes. The technology and technological challenges used for such a quantification are addressed in the following sections.

Segmentation

Segmentation is not a trivial task, because MR images are not perfect and suffer from low resolution (compared to the small structure of the hippocampus), noise and sometimes image artefacts. Therefore, a quantitative comparison and validation of segmentations is needed. For such a validation the delineated segmentation needs to be compared to a “ground truth”, but in medical image analysis of in vivo acquired brain data an unambiguous “ground truth” does not exist. Thus, manual hippocampus outlining by a trained expert is often used for validation and regarded as the “gold standard” [39,40]. A designated expert would be for instance a neuroradiologist or a trained radiology technician. Due to similar grey value intensities of adjacent brain structures such as the amygdala [41], identifying borders of the hippocampus, or other structures, is a challenging task and even trained experts can have difficulties to outline such structures. Therefore, manual segmentation is subjective and a different or even the same delineation expert might not be able to reproduce the segmentation task precisely. Furthermore, manual segmentation is labour intensive and time-consuming.

To overcome these problems, automatic and semi-automatic segmentation methods have been developed over the last decades. These can be intensity-base, atlas-based, surface-based or a combination of the categories [42]. Intensity-based methods use the intensity histogram of an MR image and classify voxels in tissue classes such as white matter (WM), grey matter (GM) and cerebrospinal fluid (CSF). Methods such as thresholding, region growing, probabilistic classification or clustering are intensity-based and are used to extract a region of interest (ROI) [42]. For classification, usually atlases and atlas registration are required. In atlas-based methods brain structures need to be segmented manually on template brains. Atlas-based methods can be divided into single, multiple and probabilistic atlas

segmentation methods [43]. In multi-atlas segmentation methods multiple atlases are registered to a target image and labels are fused to obtain the segmentation of the target space using some sort of scoring system. For probabilistic atlas segmentation methods, *a priori* probabilities of structures of interests are determined by registering a set of atlases to a standard space.

Surface-based methods are based on deformable models which use parametric curves or surfaces defined in the image domain. These are deformed under the influence of virtual internal and external forces which are computed from the image data to delineate boundaries of a ROI. Semi-automatic methods are often based on deformable models, atlas-based registration or intensity-based classification. Either initial contours need to be delineated before the deformation process takes place, or seed points in the ROI need to be selected for atlas registration or initially tissue classified images need to be post processed. For a more detailed description of such segmentation methods the reader is referred to these review articles [42–44] of which Dill et al. specifically reviews hippocampus segmentation methods.

Semi-automatic and automatic segmentation methods are usually based on manually segmented datasets, are often computationally expensive and are prone to errors arising from image noise, artefacts and anatomical abnormalities in the image. Researching, improving and developing the segmentation task is an important part of this thesis. In particular, hybrid methods that improve the speed of supervised (manual) methods are needed.

Segmentation sensitivity

Average hippocampal volume measured on MRI varies between $2cm^3$ and $6cm^3$ depending on the subject's condition and on the segmentation protocol [40,45]. This means that 1% to 4% hippocampal atrophy is quite a small amount in terms of absolute volume, and therefore segmentations need to have high accuracy. For instance, 1% hippocampal atrophy of a hippocampus with $3000mm^3$ is $30mm^3$, only 30 voxels if voxel dimensions are $1x1x1mm^3$. Usually, MRI scans do not have isotropic $1x1x1mm^3$ voxels which makes the segmentation task even more challenging. Therefore, segmentation methods need to be highly accurate to detect such subtle changes. To demonstrate this subtle change in another way, one can think of a sphere with a volume of $3000mm^3$, a radius of 8.95mm and a surface area of $1005.92mm^2$. A $30mm^3$ volume decrease of the sphere leads to a radius decrease of 0.03mm, indicating that for accurate measurement of hippocampal atrophy we need to measure a sub-millimetre surface change.

Despite being a time-consuming and difficult task, for many clinical trials segmentations were performed manually as for instance in [46–48]. It seems

unlikely that such small volume changes can be detected by an expert observer, because the human segmentation error might be higher than the volume change to be measured. However, developing robust and accurate automatic segmentation methods is a challenging problem and automatic methods were lacking clinical practice to be used in such trials [49]. In the following chapters, the performance of automatic segmentation methods in comparison to manual segmentations will be discussed in more detail. Nevertheless, reducing the time for observers to segment anatomical structures and hence reduce costs for such trials is highly important. To address this problem, a semi-automatic segmentation method was developed and will be presented in chapter 4. In the following, other image registration methods to compare segmentations and 3D rendering of labelled images will be briefly explained, because these methodologies are important for every chapter.

Registration

For atlas-based segmentation methods, image registration is needed. In image registration one image is the fixed or target image $I_T(x)$ and the other the moving or source image $I_S(x)$ with $x \in \Omega$, the image domain. Finding the transformation $T(x) = x + u(x)$, with $u(x)$ being the displacement, that spatially aligns $I_S(x)$ to $I_T(x)$ is defined as the registration problem [50]. Minimizing a cost function $\mathcal{C}$ with respect to T yields the image alignment problem:

$$\hat{T} = \arg\min_{T} \mathcal{C}(T; I_T, I_S) \tag{1}$$

Commonly, the transformation model T is divided into rigid, affine and non-linear transformation models which are defined by the degrees of freedom of the deformation (DOF). Rigid transformation consists of 6DOF for translation and rotation and affine transformation (12DOF) includes scaling and shearing. The transformation model can be expressed as:

$$T(\boldsymbol{x}) = A\boldsymbol{x} + \boldsymbol{t} \tag{2}$$

where $\mathbf{t}$ is the 3D translation vector and A is a transformation matrix consisting of 9 entries, giving 12 DOF in total. A non-linear registration has more DOF than 12 and varies across space.

Segmentation comparison

Segmentation methods are usually validated by comparison to a reference set of “gold standard” segmentations. Different segmentation comparison methodologies can be used to validate the quality of segmentations. Commonly, volumes of manual segmentations are compared to volumes of automated segmentations. The volume

of a structure can be obtained by counting the number of segmented voxels and multiplying it with the voxel dimensions. Other common comparison methods to determine the segmentation quality and reproducibility are for instance overlap, distance and correlation measurements [51]. Throughout this thesis the following comparison methods will appear. The Dice similarity coefficient is defined as:

$$DICE(V_A, V_B) = \frac{2|V_{A \cap B}|}{|V_A| + |V_B|} \tag{3}$$

in which V_A and V_B specify the volumes of segmentations A and B, respectively. These structures can be defined as sets of labelled voxels in a scan, or they can be represented by the interior of a closed (triangulated) surface. Similarly, the Jaccard similarity coefficient can be used:

$$Jacc(V_A, V_B) = \frac{|V_A \cap V_B|}{|V_A \cup V_B|} \tag{4}$$

The Dice coefficient can be converted to the Jaccard coefficient with the following formula:

$$Jacc = \frac{DICE}{(2 - DICE)} \tag{5}$$

To compare the overlap of segmentations for multiple methods or observers the Jaccard index can be generalized with:

$$CI_{gen} = \frac{\sum_{pairs\ ij} |V_i \cap V_j|}{\sum_{pairs\ ij} |V_i \cup V_j|} \tag{6}$$

in which CI_{gen} stands for generalized conformity index [52].

For volume comparison the intra-class correlation coefficient (ICC) is often used. The ICC is typically defined as the ratio of the variance of interest over the sum of the variance of interest plus the measurement error and it can take different forms depending on the statistical model [53]. Furthermore, this reliability measure is often differentiated between consistency or absolute agreement. In ICC with absolute agreement repetition variability is also considered. Such formulas and computations are discussed in depth in [53].

In linear regression, the Pearson correlation coefficient (r) and/or coefficient of determination (R^2) are used to determine how well two sets of data are related.

These are also usually used to compare volume quantities and are defined as

$$r = \frac{\sum_{i=1}^{n}(f_i - \bar{f})(y_i - \bar{y})}{\sqrt{\sum_{i=1}^{n}(f_i - f)^2}\sqrt{\sum_{i=1}^{n}(y_i - \bar{y})^2}}$$
$$R^2 = 1 - \frac{\sum_{i=1}^{n}(y_i - f_i)^2}{\sum_{i=1}^{n}(y_i - \bar{y})^2} \quad (7)$$

with f being the model prediction and y being the true data from dataset $\{y_1,\ldots,y_n\}$ with corresponding means $\bar{f}$ and $\bar{y}$. To measure the accuracy of predictions from a regression line the standard error of the estimate is often reported:

$$\sigma_{est} = \sqrt{\frac{\sum_{i=1}^{n}(y_i - f_i)^2}{n-2}} \quad (8)$$

In this formula 2 is subtracted from the number of observations n because both the slope and intercept were estimated to minimize the sum of squares.

Surface extraction

To compute an overlap index of segmentations, these should have been outlined on the same coordinate grid, i.e. segmentations should be delineated on the same image and have same voxel positions. When segmentations do not share the same coordinate grid, for instance when they are outlined on different MRI scans, these segmentations need to be mapped to each other using registration. The mapping procedure leads to interpolation errors, implying that shape and volume of the segmented structure will not be preserved. To avoid these interpolation errors, in this thesis all segmentations were converted to 3D triangulated meshes. Registration transformations can then be directly applied to the mesh points and Dice coefficients can be computed over surfaces to avoid interpolation errors. A triangulated mesh *M* is a collection of triangles and consists of a set of vertices [54]

$$\mathcal{V} = \{v_1, \ldots, v_V\} \quad (9)$$

and a set of triangular faces

$$\mathcal{F} = \{f_1, \ldots, f_F\}, \qquad \subset \mathcal{V} \times \mathcal{V} \times \mathcal{V} \quad (10)$$

The embedding of a triangulated mesh in $\mathbb{R}^3$ is specified by giving each vertex $v_i \in \mathcal{V}$ a 3D position. Then each face $f \in \mathcal{F}$ corresponds to three vertices which are part a triangle.

The extraction of a mesh from a labelled segmentation image, essentially is a form of isosurface extraction. In this thesis, the marching cube algorithm is used [55] for that goal. Marching cubes is a grid-based method in which a cube is created from the centre points of eight neighbouring voxels. This cube “marches” in steps of one voxel over the 3D scan and at each step it is determined which surface intersections need to be added for that cube. Surface intersections are found by assigning zeros and ones to the vertices at the cube depending on if the vertices are inside or outside of the surface. For instance, in the case of a labelled segmentation, vertices of the cube are assigned with a one if they belong to the segmentation. A surface patch is then created out of the intersection points which can be obtained from a triangulation look-up table. The 15 base configurations from the look-up table are illustrated in Fig. 4, in total there are $2^8 = 256$ combinations, which can be obtained by rotation, reflection and inversion of those 15 base configurations [54]. The final reconstructed surface is obtained by assembling all triangles detected for each cube position.

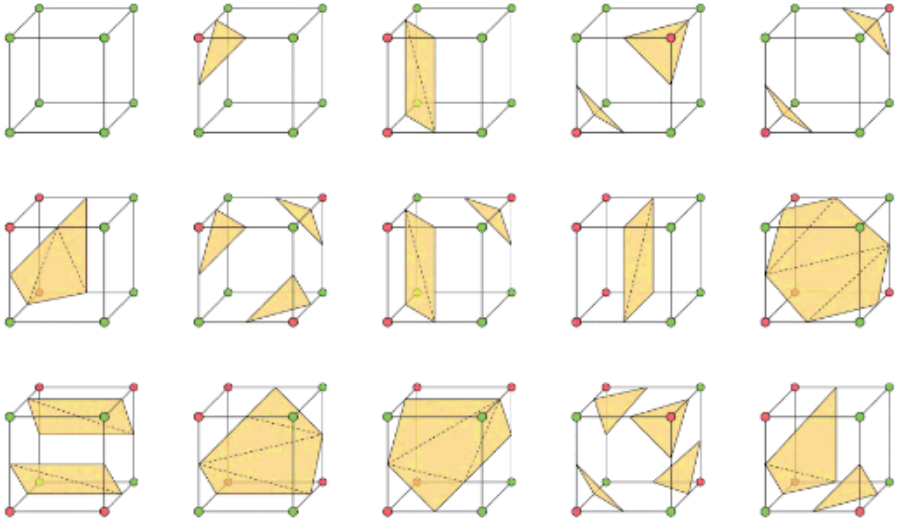

Fig. 4: The 15 basic configurations of the marching cubes triangulation table. The other formations from the look-up table can be found by rotation, reflection or inversion. Ref: [54] p. 17.

The volume of a mesh can be calculated by creating tetrahedrons out of the triangles and the origin [56]. These tetrahedron volumes are either negative or positive depending on the inwards or outwards orientation of the triangle normal vectors.

The tetrahedron volume of three vertices (v_1, v_2, v_3) and origin O in $\mathbb{R}^3$ is defined as:

$$V_{Ov_1v_2v_3} = \frac{1}{6}|(v_1 \times v_2) \cdot v_3| \quad (11)$$

Summing up the signed tetrahedron volumes and taking the absolute value of the summation yields the volume of the surface.

The shape and volume of the surface representation of an object will be slightly different from its representation by image voxels because the marching cubes algorithm rounds off corners. Nevertheless, in this thesis all labelled images are converted to meshes prior to processing to avoid interpolation errors resulting from the image co-registration process.

To quantify the difference between the two representations in relation to the interpolation error a small simulation study was performed. A total of 360 hippocampi were segmented on slightly rotated T1-weighted MRI. Using linear registration and nearest neighbour interpolation the segmentations were mapped back to their original space. The interpolation error was quantified by calculating the percentage volume difference between the original and interpolated segmentations. The original hippocampus segmentations were also converted to meshes. Applying linear registration on those meshes would lead to zero errors, but to quantify the change resulting from mesh conversion the percentage volume difference between meshes and voxel-wise segmentations was calculated. The results can be seen in Fig. 5, which shows that volumes of the meshes have much smaller variability in the difference in volume compared to interpolated segmentations. The standard error due to interpolation is of the same order of magnitude as the expected atrophy rate (1-3%). However, the boxplot illustrates that mesh volumes are smaller than the original segmentations, which is the result of creating meshes from the voxel-wise labelled segmentations. This might seem disadvantageous compared to interpolated segmentations, which are centred around zero, but volume reduction due to mesh conversion is systematic. The following test shows that this systematic bias cancels when determining hippocampal atrophy rates. Using the same dataset, hippocampal atrophy rates of 160 longitudinal segmentations were determined and atrophy rates measured with the original segmentations were plotted against atrophy rates measured with the interpolated segmentations and against atrophy rates measured with the meshes (Fig. 6). The advantage of using meshes is evident from Fig. 6 - atrophy rates are maintained when converting segmentations to meshes.

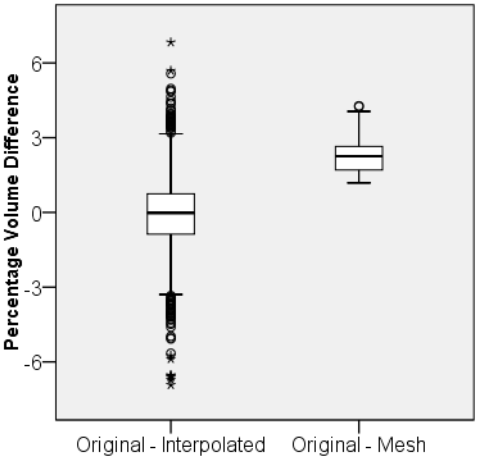

Fig. 5: Comparing the volume effect of interpolation and conversion to meshes. Mean and standard deviation between original and interpolated segmentations was -0.09(±1.954) and between original and mesh segmentation it was 2.26(±0.626).

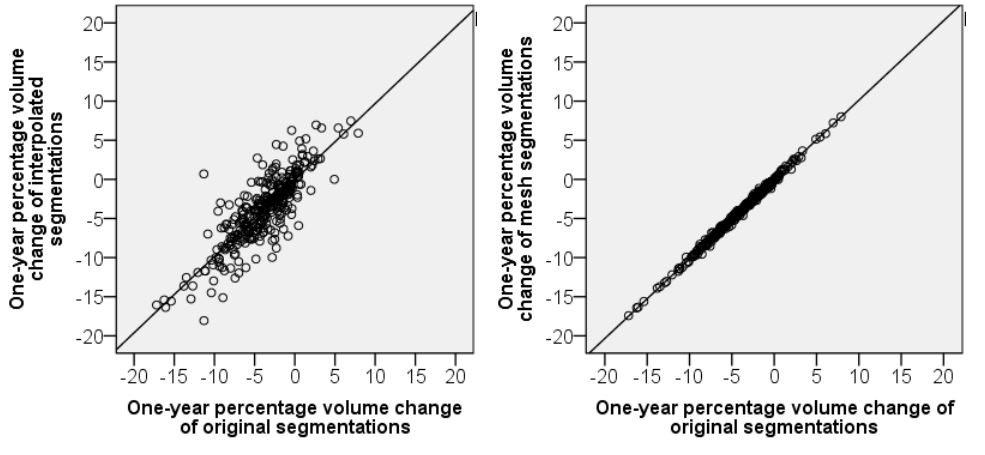

Fig. 6: From 160 longitudinal hippocampus segmentations one-year hippocampal atrophy rates were measured. Atrophy rates measured with the original segmentations was plotted against atrophy rates measured with the interpolated segmentations (left; R^2=0.701) and against atrophy rates measured with the meshes (right; R^2= 0.996). The lines are identity lines.

1.3. Aim of this thesis

The general objective of this thesis was to optimize methods for hippocampus segmentation and atrophy measurements in the field of neuroradiology and radiotherapy. Within the scope of the general objective, the performance of commonly used available automatic segmentation methods are compared and tested. Furthermore, segmentation and atrophy differences are analyzed to determine regions that are difficult to outline and regions in which hippocampal atrophy takes place the most. With the labour intensiveness of current manual delineation protocols in mind, a semi-automatic hippocampus segmentation method is developed which reduces the segmentation time for expert raters. This method is tested for broader applicability to be used for segmenting subcortical brain structures and for hippocampus delineation in radiotherapy. Finally, the method with the best statistical power in atrophy measurement is determined.

Overview of this thesis

Over the last few decades, hippocampal volumes have been determined manually and automatically. It is therefore important to quantify differences between manual segmentations and automatic segmentation methods. In **Chapter 2** regional hippocampal volume differences were systematically investigated and differences between two frequently used automatic segmentation methods and manual hippocampus segmentations were determined.

In radiotherapy, hippocampus delineation gained importance in the last 10 years. The hippocampus delineation is used to develop brain radiation treatment plans in which the dose to the hippocampus is kept to a minimum. **Chapter 3** analyses delineation variability of multiple observers who followed a relatively new segmentation protocol.

In **Chapter 4** a new semi-automatic delineation method to reduce segmentation time is proposed. This delineation method is based on mesh-processing procedures and is therefore called FAst Segmentation Through SURface Fairing (FASTSURF). For validation, FASTSURF hippocampus segmentations are compared with manual segmentations and automatic segmentation methods.

In MS GM atrophy occurs and analysing GM atrophy of the caudate nucleus, putamen and thalamus is of particular interest because of the relation of subcortical GM atrophy to disability and cognitive decline. In **Chapter 5** FASTSURF segmentation accuracy of these structures is investigated and parameters are optimized to lay the foundation for a follow-up study in which FASTSURF will be used to create “gold standard” segmentations.

Atrophy can be determined by manually segmenting structures on longitudinal MRI scans or with automatic methods. In **Chapter 6** hippocampal atrophy in the presence of AD is determined using manual segmentations and seven automatic methods, focusing on registration-based methods. These were compared and the power of using such methods to determine short-term hippocampal volume loss compared.

References

[1] Jenkinson M, Beckmann CF, Behrens TEJ, Woolrich MW, Smith SM. FSL. Neuroimage 2012;62:782–90.

[2] Grabner G, Janke AL, Budge MM, Smith D, Pruessner J, Collins DL. Symmetric atlasing and model based segmentation: an application to the hippocampus in older adults. Med Image Comput Comput Assist Interv Int Conf Med Image Comput Comput Assist Interv 2006;9:58–66.

[3] Winterburn JL, Pruessner JC, Chavez S, Schira MM, Lobaugh NJ, Voineskos AN, et al. A novel in vivo atlas of human hippocampal subfields using high-resolution 3T magnetic resonance imaging. Neuroimage 2013;74:254–65.

[4] Amaral RSC, Park MTM, Devenyi GA, Lynn V, Pipitone J, Winterburn J, et al. Manual segmentation of the fornix, fimbria, and alveus on high-resolution 3T MRI: Application via fully-automated mapping of the human memory circuit white and grey matter in healthy and pathological aging. Neuroimage 2018;170:132–50.

[5] Ramachandran VS. Encyclopedia of human behavior. 2nd ed. Elsevier/Academic Press; 2012.

[6] Leuner B, Gould E. Structural plasticity and hippocampal function. Annu Rev Psychol 2010;61:111–40, C1-3.

[7] Bertram L, Tanzi RE. The genetic epidemiology of neurodegenerative disease. J Clin Invest 2005;115:1449–57.

[8] Qiu C, Kivipelto M, von Strauss E. Epidemiology of Alzheimer's disease: occurrence, determinants, and strategies toward intervention. Dialogues Clin Neurosci 2009;11:111–28.

[9] Prince M, Wimo A, Guerchet M, Ali G-C, Wu Y-T, Prina M. The Global Impact of Dementia AN ANALYSIS OF PREVALENCE, INCIDENCE, COST AND TRENDS. London: 2015.

[10] Scheltens P, Blennow K, Breteler MMB, de Strooper B, Frisoni GB, Salloway S, et al. Alzheimer's disease. Lancet 2016;388:505–17.

[11] Petersen RC. Mild cognitive impairment as a diagnostic entity. J. Intern. Med., vol. 256, 2004, p. 183–94.

[12] Gauthier S, Reisberg B, Zaudig M, Petersen RC, Ritchie K, Broich K, et al. Mild cognitive impairment. Lancet (London, England) 2006;367:1262–70.

[13] Pini L, Pievani M, Bocchetta M, Altomare D, Bosco P, Cavedo E, et al. Brain atrophy in Alzheimer's Disease and aging. Ageing Res Rev 2016;30:25–48.

[14] Calabrese M, Magliozzi R, Ciccarelli O, Geurts JJG, Reynolds R, Martin R. Exploring the origins of grey matter damage in multiple sclerosis. Nat Rev Neurosci 2015;16:147–58.

[15] Geurts JJ, Calabrese M, Fisher E, Rudick RA. Measurement and clinical effect of grey matter pathology in multiple sclerosis. Lancet Neurol 2012;11:1082–92.

[16] Brück W. The pathology of multiple sclerosis is the result of focal inflammatory demyelination with axonal damage. J Neurol 2005;252:v3–9.

[17] Fisher E, Lee JC, Nakamura K, Rudick RA. Gray matter atrophy in multiple sclerosis: A longitudinal study. Ann Neurol 2008;64:255–65.

[18] Schoonheim MM, Hulst HE, Brandt RB, Strik M, Wink AM, Uitdehaag BMJ, et al. Thalamus structure and function determine severity of cognitive impairment in multiple sclerosis. Neurology 2015;84:776–83.

[19] Bishop CA, Newbould RD, Lee JS, Honeyfield L, Quest R, Colasanti A, et al. Analysis of ageing-associated grey matter volume in patients with multiple sclerosis shows excess atrophy in subcortical regions. NeuroImage Clin 2017;13:9–15.

[20] Sicotte NL, Kern KC, Giesser BS, Arshanapalli A, Schultz A, Montag M, et al. Regional hippocampal atrophy in multiple sclerosis. Brain 2008;131:1134–41.

[21] Cash DM, Rohrer JD, Ryan NS, Ourselin S, Fox NC. Imaging endpoints for clinical trials in Alzheimer's disease. Alzheimers Res Ther 2014;6:87.

[22] Fraser MA, Shaw ME, Cherbuin N. A systematic review and meta-analysis of longitudinal hippocampal atrophy in healthy human ageing. Neuroimage 2015;112:364–74.

[23] Pedraza O, Bowers D, Gilmore R. Asymmetry of the hippocampus and amygdala in MRI volumetric measurements of normal adults. J Int Neuropsychol Soc 2004;10:664–78.

[24] Barnes J, Scahill RI, Schott JM, Frost C, Rossor MN, Fox NC. Does Alzheimer's Disease Affect Hippocampal Asymmetry? Evidence from a Cross-Sectional and Longitudinal Volumetric MRI Study. Dement Geriatr Cogn Disord 2005;19:338–44.

[25] Schuff N, Woerner N, Boreta L, Kornfield T, Shaw LM, Trojanowski JQ, et al. MRI of hippocampal volume loss in early Alzheimer's disease in relation to ApoE genotype and biomarkers. Brain 2009;132:1067–77.

[26] Jack CR, Petersen RC, Xu Y, O'Brien PC, Smith GE, Ivnik RJ, et al. Rate of medial temporal lobe atrophy in typical aging and Alzheimer's disease. Neurology 1998;51:993–9.

[27] Barnes J, Bartlett JW, van de Pol LA, Loy CT, Scahill RI, Frost C, et al. A meta-analysis of hippocampal atrophy rates in Alzheimer's disease. Neurobiol Aging 2009;30:1711–23.

[28] Tabatabaei-Jafari H, Shaw ME, Cherbuin N. Cerebral atrophy in mild cognitive impairment: A systematic review with meta-analysis. Alzheimer's Dement Diagnosis, Assess Dis Monit 2015;1:487–504.

[29] Makale MT, McDonald CR, Hattangadi-Gluth JA, Kesari S. Mechanisms of radiotherapy-associated cognitive disability in patients with brain tumours. Nat Rev Neurol 2016;13:52–64.

[30] Greene-Schloesser D, Robbins ME, Peiffer AM, Shaw EG, Wheeler KT, Chan MD. Radiation-induced brain injury: A review. Front Oncol 2012;2:73.

[31] Lee YW, Cho HJ, Lee WH, Sonntag WE. Whole brain radiation-induced cognitive impairment: pathophysiological mechanisms and therapeutic targets. Biomol Ther (Seoul) 2012;20:357–70.

[32] Ferrer I, Serrano T, Alcantara S, Tortosa A, Graus F. X-ray-induced cell death in the developing hippocampal complex involves neurons and requires protein synthesis. J Neuropathol Exp Neurol 1993;52:370–8.

[33] Raber J, Rola R, LeFevour A, Morhardt D, Curley J, Mizumatsu S, et al. Radiation-induced cognitive impairments are associated with changes in indicators of hippocampal neurogenesis. Radiat Res 2004;162:39–47.

[34] Nagai R, Tsunoda S, Hori Y, Asada H. Selective vulnerability to radiation in the hippocampal dentate granule cells. Surg Neurol 2000;53:503-6; discussion 506-7.

[35] Madsen TM, Kristjansen PEG, Bolwig TG, Wörtwein G. Arrested neuronal proliferation and impaired hippocampal function following fractionated brain irradiation in the adult rat. Neuroscience 2003;119:635–42.

[36] Mizumatsu S, Monje ML, Morhardt DR, Rola R, Palmer TD, Fike JR. Extreme sensitivity of adult neurogenesis to low doses of X-irradiation. Cancer Res 2003;63:4021–7.

[37] Gondi V, Tomé WA, Mehta MP. Why avoid the hippocampus? A comprehensive review. Radiother Oncol 2010;97:370–6.

[38] Gondi V, Pugh SL, Tome WA, Caine C, Corn B, Kanner A, et al. Preservation of memory with conformal avoidance of the hippocampal neural stem-cell compartment during whole-brain radiotherapy for brain metastases (RTOG 0933): A phase II multi-institutional trial. J Clin Oncol 2014;32:3810–6.

[39] Barnes J, Foster J, Boyes RG, Pepple T, Moore EK, Schott JM, et al. A comparison of methods for the automated calculation of volumes and atrophy rates in the hippocampus. Neuroimage 2008;40:1655–71.

[40] Boccardi M, Ganzola R, Bocchetta M, Pievani M, Redolfi A, Bartzokis G, et al. Survey of protocols for the manual segmentation of the hippocampus: Preparatory steps towards a joint EADC-ADNI harmonized protocol. Adv Alzheimer's Dis 2011;2:111–25.

[41] Fischl B, Salat DH, Busa E, Albert M, Dieterich M, Haselgrove C, et al. Whole brain segmentation: Automated labeling of neuroanatomical structures in the human brain. Neuron 2002;33:341–55.

[42] Despotović I, Goossens B, Philips W. MRI segmentation of the human brain: challenges, methods, and applications. Comput Math Methods Med 2015;2015:450341.

[43] Dill V, Franco AR, Pinho MS. Automated methods for hippocampus segmentation: the evolution and a review of the state of the art. Neuroinformatics 2015;13:133–50.

[44] González-Villà S, Oliver A, Valverde S, Wang L, Zwiggelaar R, Lladó X. A review on brain structures segmentation in magnetic resonance imaging. Artif Intell Med 2016;73:45–69.

[45] Geuze E, Vermetten E, Bremner JD. MR-based in vivo hippocampal volumetrics: 2. Findings in neuropsychiatric disorders. Mol Psychiatry 2005;10:160–84.

[46] Wilkinson D, Fox NC, Barkhof F, Phul R, Lemming O, Scheltens P. Memantine and brain atrophy in alzheimer's disease: A 1-year randomized controlled trial. J Alzheimer's Dis 2012;29:459–69.

[47] Dodel R, Rominger A, Bartenstein P, Barkhof F, Blennow K, Förster S, et al. Intravenous immunoglobulin for treatment of mild-to-moderate Alzheimer's disease: A phase 2, randomised, double-blind, placebo-controlled, dose-finding trial. Lancet Neurol 2013;12:233–43.

[48] Quinn JF, Raman R, Thomas RG, Yurko-Mauro K, Nelson EB, Van Dyck C, et al. Docosahexaenoic acid supplementation and cognitive decline in Alzheimer disease: A randomized trial. JAMA - J Am Med Assoc 2010;304:1903–11.

[49] Lötjönen J, Wolz R, Koikkalainen J, Julkunen V, Thurfjell L, Lundqvist R, et al. Fast and robust extraction of hippocampus from MR images for diagnostics of Alzheimer's disease. Neuroimage 2011;56:185–96.

[50] Klein S, Staring M, Murphy K, Viergever MA, Pluim JPW. elastix: a toolbox for intensity-based medical image registration. IEEE Trans Med Imaging 2010;29:196–205.

[51] Taha AA, Hanbury A. Metrics for evaluating 3D medical image segmentation: Analysis, selection, and tool. BMC Med Imaging 2015;15:29.

[52] Kouwenhoven E, Giezen M, Struikmans H. Measuring the similarity of target volume delineations independent of the number of observers. Phys Med Biol 2009;54:2863–73.

[53] Shrout PE, Fleiss JL. Intraclass Correlation: Uses in Assessing Rater Reliabitlity. Psychol Bull 1979;86:420–8.

[54] Botsch M, Kobelt L, Pauly M, Alliez P, Levy B. Polygon Mesh Processing. vol. 1. A K Peters; 2010.

[55] Lorensen WE, Cline HE. Marching cubes: A high resolution 3D surface construction algorithm. Proc. 14th Annu. Conf. Comput. Graph. Interact. Tech. - SIGGRAPH '87, New York, New York, USA: ACM Press; 1987, p. 163–9.

[56] Cha Zhang, Tsuhan Chen. Efficient feature extraction for 2D/3D objects in mesh representation. Proc. 2001 Int. Conf. Image Process. (Cat. No.01CH37205), vol. 2, IEEE; 2001, p. 935–8.